IOPscience iopscience.iop.org

Home Search Collections Journals About Contact us My IOPscience

Detailed ferromagnetic resonance study of amorphous Fe-rich $Fe_{90-x}Co_xZr_{10}$ alloys. II: critical behaviour and uniaxial anisotropy

This article has been downloaded from IOPscience. Please scroll down to see the full text article.

1996 J. Phys.: Condens. Matter 8 4567

(http://iopscience.iop.org/0953-8984/8/25/013)

View the table of contents for this issue, or go to the journal homepage for more

Download details:
IP Address: 171.66.16.151
The article was downloaded on 12/05/2010 at 22:55

Please note that terms and conditions apply.

J. Phys.: Condens. Matter **8** (1996) 4567–4588. Printed in the UK

Detailed ferromagnetic resonance study of amorphous Fe-rich $Fe_{90-x}Co_xZr_{10}$ alloys. II: critical behaviour and uniaxial anisotropy

V Siruguri† and S N Kaul‡

School of Physics, University of Hyderabad, Central University PO, Hyderabad-500 046, India

Received 4 January 1996

Abstract. Contrary to the earlier reports, a detailed ferromagnetic resonance (FMR) study of amorphous $Fe_{90-x}Co_xZr_{10}$ alloys with $0 \leqslant x \leqslant 10$ in the critical region shows that the critical exponents β and γ for spontaneous magnetization and initial susceptibility, which characterize the ferromagnetic (FM)–paramagnetic (PM) phase transition at the Curie temperature T_C, possess values that are *independent* of composition and close to those predicted for a three-dimensional isotropic nearest-neighbour Heisenberg ferromagnet. The fraction c of spins that participates in the FM–PM phase transition has a value of 11% for the alloy with $x = 0$ and increases with increasing Co concentration x as $c(x) - c(0) \simeq ax^2$. In the critical region, the Landau–Lifshitz–Gilbert relaxation mechanism dominantly contributes to the 'peak-to-peak' FMR linewidth ΔH_{pp} and hence $\Delta H_{pp}(T) \propto [M_S(T)]^{-1}$, where M_S is the saturation magnetization. Consistent with the results obtained in a wide temperature range, which embraces the critical region, the Landé splitting factor g has a temperature- and composition-independent value of 2.07 ± 0.02 while the Gilbert damping parameter λ, although temperature independent, decreases with increasing Co concentration. The angular dependence of the resonance field H_{res} observed in both 'in-plane' and 'out-of-plane' sample geometries has been fitted to theoretical expressions that take into account the uniaxial anisotropy. The uniaxial anisotropy field $H_k = 2K_u/M_S$ increases with increasing Co concentration and scales with M_S. That the uniaxial anisotropy has its origin in the pseudo-dipolar atomic pair ordering is vindicated by the finding that $K_u \propto M_S^2$.

1. Introduction

During the past decade, a number of experimental techniques such as bulk magnetization [1–5], AC susceptibility [6, 7], electrical resistivity [8, 9], small-angle neutron scattering [10, 11] and ferromagnetic resonance (FMR) [12–14] have been used to investigate the critical behaviour of amorphous (a-)Fe-rich $Fe_{100-x}Zr_x$ ($8 \leqslant x \leqslant 11$) alloys near the ferromagnetic (FM)–paramagnetic (PM) phase transition. However, different techniques have yielded widely different [5, 6] (differing by as much as 50%) values for the critical exponents that characterize the FM–PM phase transition at the Curie point T_C. A wide disparity of the same type also exists between the results of bulk magnetization [3] and FMR [13] measurements on a-$Fe_{90-x}Co_xZr_{10}$ alloys. Subsequent attempts [4, 5, 7] to get at the root of this discrepancy, particularly in the case of a-$Fe_{100-x}Zr_x$ alloys, revealed that the results of different measurements conform well with one another when the serious flaws

† Present address: Inter University Consortium—Bombay Centre, Solid State Physics Division, Bhabha Atomic Research Centre, Trombay, Bombay-400 085, India.

‡ Author to whom all correspondence should be addressed.

0953-8984/96/254567+22$19.50 © 1996 IOP Publishing Ltd

[5, 9] (basically responsible for the abnormally large [2, 3, 8] exponent values) in the previous data analysis [2, 3, 8] are eliminated in the re-analysis [5, 9]. This observation strongly suggests that a careful analysis of accurate data taken in the critical region might resolve the controversy surrounding the nature of FM–PM phase transition in a-$Fe_{90-x}Co_xZr_{10}$ alloys as well. With this understanding, a detailed FMR investigation of the FM–PM phase transition in these glassy alloys was undertaken. We have previously used the FMR technique to determine critical exponents for some of the compositions [13] in the above-mentioned alloy series. The present study, however, goes far beyond the previous study in that the FMR spectra are taken at much closer temperature intervals in the critical region, measurements have been performed over an extended Co concentration range and the Curie temperature for each composition is approached more closely than in the earlier experiments [13] by achieving better temperature control and substantial reduction in the temperature gradient along the sample length. As a result of these improvements, more accurate estimates of the critical exponents and amplitudes are obtained.

With a view to gaining more physical insight into the nature of magnetic ordering in a-$Fe_{90-x}Co_xZr_{10}$ alloys, magnetic anisotropy in this alloy system has been investigated in detail by measuring the temperature and angular dependences of the (FM) resonance field. This study reveals that the anisotropy is of the uniaxial type and the uniaxial anisotropy field H_k *scales* with the saturation magnetization M_S over a wide temperature range for all the compositions investigated in the above alloy series. Values of M_S and H_k at $T = 0.6T_C$ for different compositions deduced from the lineshape analysis of the FMR spectra taken at this temperature conform well with those extracted from the angular dependence of the resonance field. The physical implications of these results are discussed in detail in section 3.

2. Experimental details

As the details concerning sample preparation, characterization and the measurement procedure have already been given in the preceding paper [15] (henceforth referred to as I), they are not repeated here. FMR measurements at a fixed microwave frequency of 9.23 GHz were performed using sample configurations the same as those mentioned in I, i.e. the horizontal-parallel ($\|^h$) and vertical-parallel ($\|^v$) configurations. The microwave power absorption derivative (PAD) $\mathrm{d}P/\mathrm{d}H$ as a function of external static magnetic field for a given sample configuration was measured at 0.3 K intervals in the critical region, i.e. in the temperature range $-0.1 \lesssim \epsilon = (T - T_C)/T_C \lesssim 0.1$. At every temperature setting, the sample temperature was maintained constant to within ± 30 mK by means of a proportional, integral and differential temperature controller. The Curie temperature T_C could be approached more closely (i.e. the deviation of the closest temperature from T_C divided by T_C could be reduced by an order of magnitude) in the present experiments because of improved temperature control and substantial reduction in the temperature gradient along the sample length brought about by the helium exchange gas in the sample tube. The sample temperature was measured by a pre-calibrated copper–constantan therocouple in direct contact with the sample.

The FMR field and linewidth were measured as functions of the angle between the external static magnetic field H_{ex} direction and the sample plane or between the H_{ex} direction and easy direction within the sample plane with the aid of a goniometer attachment (mounted on the microwave cavity) which enabled rotation and orientation of the sample plane at specific angles with respect to the direction of H_{ex}. Two different sample configurations, i.e. 'in-plane' (IP) and 'out-of-plane' (OP) configurations, were used. In the IP configuration, H_{ex} can have any direction within the sample plane whereas, in the OP geometry, H_{ex} can

be oriented at any angle in the range 0–180° with respect to the sample plane. PAD curves were recorded at different angles in each of the two sample configurations at $T = 0.6T_C$.

3. Data analysis, results and discussion

3.1. Critical behaviour

The continuous curves in figure 1 depict the observed functional dependence of $\mathrm{d}P/\mathrm{d}H$ on H in the $\|^h$ configuration at a few selected values of temperature in the critical region. These curves are also representative of those recorded for a-$Fe_{88}Co_2Zr_{10}$ in the $\|^v$ configuration and for other compositions in the amorphous alloy series a-$Fe_{90-x}Co_xZr_{10}$ in both $\|^h$ and $\|^v$ geometries. In this figure, open circles denote the theoretical variation in $\mathrm{d}P/\mathrm{d}H$ with H for the primary resonance yielded by equations (1)–(3) of I for the choice of the Landé splitting factor g and saturation magnetization M_S, that optimizes agreement with the experimental variation. Such a detailed lineshape analysis, carried out for each PAD curve separately, not only permits an accurate determination of $M_S(T)$ but also reveals that the Landau–Lifshitz–Gilbert (LLG) equation of motion for magnetization (which forms the basis for equation (2) of I) adequately describes the resonant behaviour in the critical region and that g has a fixed value of 2.07 ± 0.02 within the temperature and concentration ranges investigated.

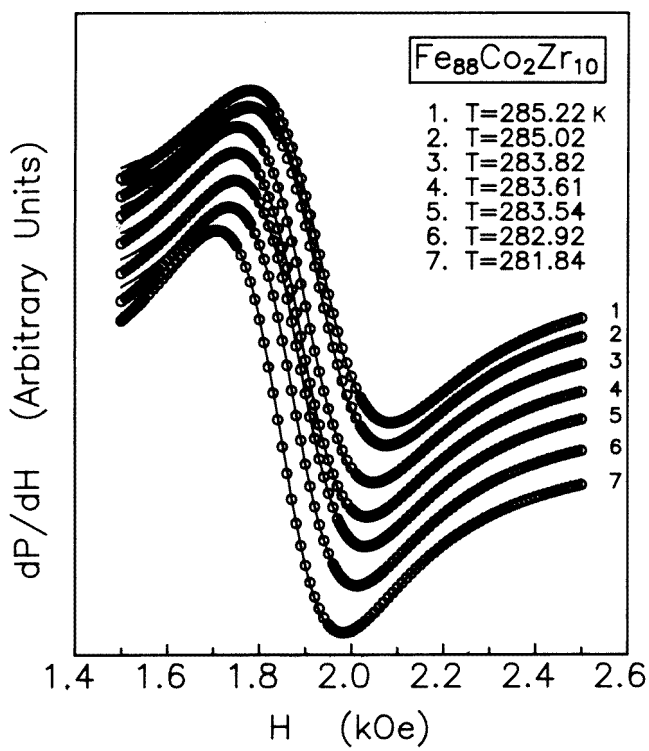

Figure 1. PAD curves for a-$Fe_{88}Co_2Zr_{10}$ alloy at a few representative temperature values in the critical region recorded in the horizontal-parallel sample configuration. Solid curves depict the observed variation of $\mathrm{d}P/\mathrm{d}H$ with H whereas the open circles denote the calculated values on equations (1)–(3) of I.

Table 1. A comparison of the experimentally determined values of the critical exponents and amplitude ratios for a-$Fe_{90-x}Co_xZr_{10}$ alloys with the theoretical estimates for a 3D Heisenberg ferromagnet. The numbers in parentheses denote the uncertainty in the least significant figure.

Concentration x	T_C (K)	β	γ	m_0 (G)	$m_0/M_S(0)$	h_0/m_0	h_0 (10^5 Oe)	μ_0 (μ_B)	$\frac{\mu_0 h_0}{k_B T_C}$	μ_{eff} (μ_B)	c (%)
0	238.50(15)	0.380(20)	1.38(3)	930(30)	0.98(4)	500(50)	4.7(6)	1.311	0.172(22)	12.0(15)	10.9(12)
1	254.50(15)	0.380(20)	1.38(3)	1075(30)	1.09(4)	400(50)	4.3(7)	1.368	0.155(23)	14.0(15)	9.8(10)
2	283.50(10)	0.380(20)	1.39(3)	1095(30)	1.09(4)	500(50)	5.5(7)	1.385	0.180(23)	12.2(15)	11.4(13)
4	335.00(10)	0.370(20)	1.38(3)	1140(30)	1.16(4)	700(50)	8.0(8)	1.365	0.218(22)	9.9(10)	13.8(12)
6	376.50(10)	0.380(20)	1.38(3)	1225(40)	1.19(5)	1000(50)	12.3(10)	1.423	0.311(25)	7.2(5)	19.8(15)
8	419.50(10)	0.375(20)	1.38(3)	1200(40)	1.13(5)	1500(50)	18.0(12)	1.465	0.422(30)	5.5(4)	26.7(18)
10	462.50(10)	0.380(20)	1.39(3)	1200(40)	1.09(4)	2200(50)	26.4(15)	1.532	0.587(35)	4.1(2)	37.2(21)
3D Heisenberg		0.365(3)[a]	1.386(4)[a]		1.22[b]				1.58[b]		

[a] From [17].
[b] From [18].

3.1.1. Scaling-equation-of-state analysis. Our earlier measurements [16] have demonstrated that the values of $M_S(T)$ deduced from the lineshape analysis are in excellent agreement with those measured on the same sample at an external magnetic field whose strength is comparable with the resonance field H_{res}. In view of this observation, H_{res} is identified with the ordering field H conjugate to M ($\equiv M_S$) and no distinction is made between the $M_S(H_{res}, T)$ data (yielded by the lineshape analysis), and the $M(H, T)$ data. The magnetic or scaling equation of state (SES) of the form

$$m = f_{\pm}(h) \tag{1}$$

is used to arrive at the correct choice of the critical exponents β and γ for spontaneous magnetization and initial susceptibility and of the Curie temperature T_C, which makes the $M(H, T)$ data in the critical region fall on two universal curves, f_- for $\epsilon < 0$ and f_+ for $\epsilon > 0$, in an m versus h plot. In equation (1), $m \equiv M/|\epsilon|^{\beta}$ and $h \equiv H/|\epsilon|^{\beta+\gamma}$ are the scaled magnetization and scaled field, respectively, $\epsilon = (T - T_C)/T_C$, and the plus and minus signs refer to temperatures above and below T_C. The choice of the parameters β, γ and T_C for an optimum collapse of the data onto the two universal curves, however, depends sensitively on the temperature range over which such a data collapse is attempted and is, therefore, not unique. Hence, a 'range-of-fit' SES analysis is used wherein the range of temperatures in an m versus h plot is progressively narrowed down by excluding more and more of the data taken at temperatures far away from T_C. In the process, the exponents β and γ become increasingly sensitive to the choice of T_C and even a slight deviation in the exponent values from the correct choice results in a strong departure of the data from the curves $f_-(h)$ and $f_+(h)$. The asymptotic values of the exponents are obtained only when they become stable against further reduction in the range of ϵ. Figure 2 serves to illustrate this fact. The best values of the parameters T_C, β and γ for the alloys with $x = 0$, 1, 2, 4, 6, 8 and 10 in the a-$Fe_{90-x}Co_xZr_{10}$ series obtained in this way are listed in table 1.

3.1.2. Critical exponents and amplitudes. Critical exponents alone do not fully characterize the critical behaviour near the FM–PM transition but they do so only in association with the corresponding critical amplitudes. Therefore, a complete understanding of the critical behaviour at T_C is achieved only when the values of critical exponents as well as critical amplitudes are determined. The values of critical amplitudes, like those of critical exponents, are extremely sensitive to the choice of T_C and hence a very high accuracy in the determination of T_C is called for. When a double-logarithmic plot of the type shown in figure 2 is used to determine the values of the exponents and T_C, the values so obtained may not be accurate enough since small deviations in the data from the universal $f_-(h)$ and $f_+(h)$ curves tend to be covered up due to the insensitive nature of the log–log scale. A more rigorous method of analysis that gets rid of these ambiguities and determines more accurately the values of the critical exponents, critical amplitudes and T_C is based on the SES form

$$m^2 = \mp a_{\pm} + b_{\pm}(h/m) \tag{2}$$

where the plus and minus signs as well as h and m have the same meaning as in equation (1). In an m^2 versus h/m plot, slight deviations that escape detection in a $\ln m$ versus $\ln h$ plot can be discerned with ease. In view of the definitions

$$M_S(\epsilon) = \lim_{H\to 0}[M(H, \epsilon)] = m_0(-\epsilon)^{\beta} \qquad \epsilon < 0 \tag{3}$$

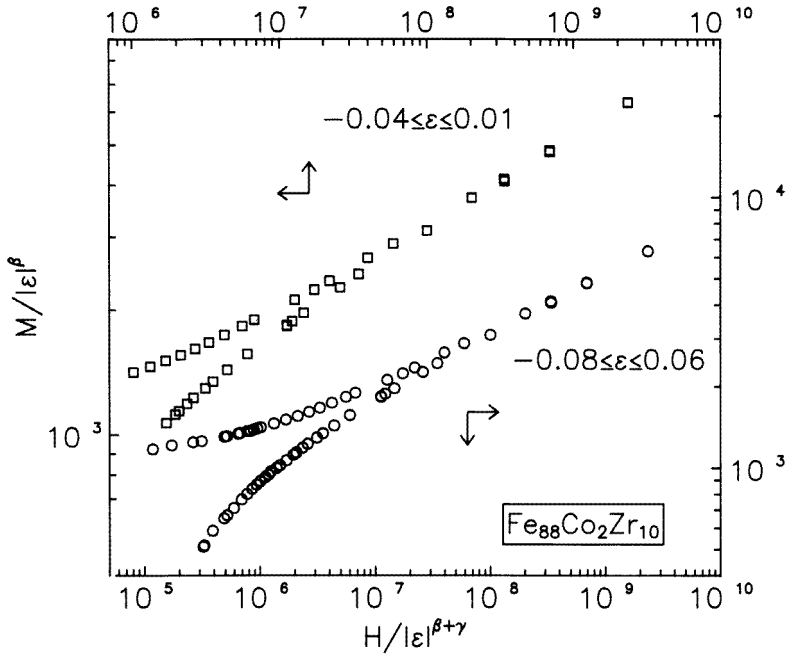

Figure 2. $\ln(M/|\epsilon|^{\beta})$ versus $\ln(H/|\epsilon|^{\beta+\gamma})$ plots for a-$Fe_{88}Co_2Zr_{10}$ alloy for the two different temperature ranges in the critical region, where $\epsilon = (T - T_C)/T_C$.

and

$$\chi_0^{-1}(\epsilon) = \left[\left|\frac{\partial M(H,\epsilon)}{\partial H}\right|_{H=0}\right]^{-1} = \left(\frac{h_0}{m_0}\right)\epsilon^{\gamma} \qquad \epsilon > 0 \tag{4}$$

the coefficients in equation (2) can be related to the critical amplitudes m_0 and h_0/m_0 as

$$a_-^{1/2} = m_0 \tag{5a}$$

and

$$a_+/b_+ = h_0/m_0. \tag{5b}$$

The intercepts of the universal curves with the m^2 and h/m axes in an m^2 versus h/m plot, therefore, give the critical amplitudes m_0^2 and h_0/m_0, respectively (figure 3). Such m^2 versus h/m plots for a-$Fe_{90-x}Co_xZr_{10}$ alloys that use the values of T_C and critical exponents obtained from the 'range-of-fit' analysis (table 1) are depicted in figure 4. The values of the critical amplitudes deduced from the m^2 versus h/m plots (figure 4) by the method illustrated in figure 3 are also displayed in table 1. It is observed from figure 4 that the experimental data fall on the universal curves without any appreciable deviations even at low fields and this implies that the values of the critical exponents and T_C are reasonably accurate. Also listed in table 1 are the ratios $m_0/M_S(0)$ and $\mu_0 h_0/k_B T_C$ (where μ_0 and $M_S(0)$ are the magnetic moment per alloy atom and saturation magnetization at 0 K, respectively; the values of $M_S(0)$, and hence of μ_0, are obtained from the spin-wave analysis described in I) which, together with the exponent values, are compared with the theoretical estimates [17, 18] predicted for an isotropic three-dimensional (3D) nearest-neighbour (NN) Heisenberg ferromagnet.

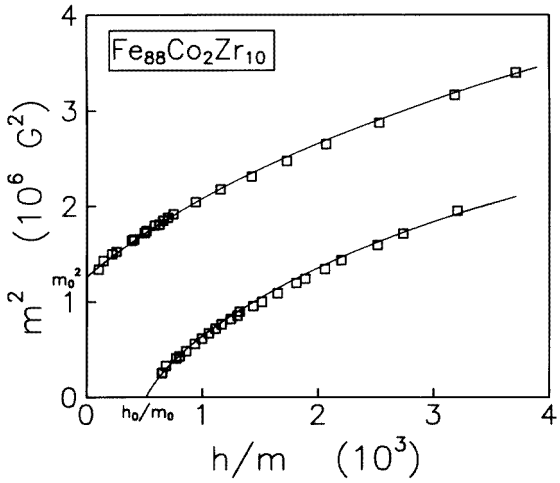

Figure 3. A subset of the data presented in figure 4 for a-Fe$_{88}$Co$_2$Zr$_{10}$ in the region of small m^2- and h/m-values replotted on a sensitive scale with a view to demonstrating the values of the intercepts m_0^2 and h_0/m_0 on m^2 and h/m axes clearly.

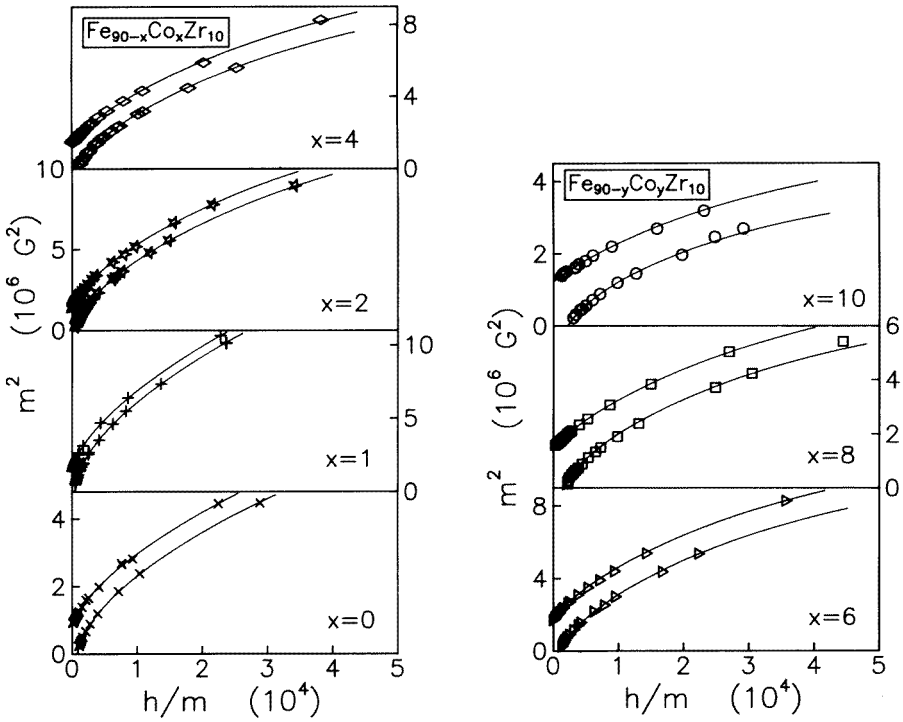

Figure 4. m^2 versus h/m plots for a-Fe$_{90-x}$Co$_x$Zr$_{10}$ alloys constructed using the M_S data deduced from the FMR spectra recorded at different temperatures in the critical region.

From the comparison between theory and experiment (table 1), it is evident that, while the experimental values of the exponents and the ratio $m_0/M_S(0)$ are in close agreement

with the theoretically predicted values, the observed value of the ratio $\mu_0 h_0/k_B T_C$ is smaller than the theoretical value by an order of magnitude for all the alloy compositions. If h_0 is presumed to be an effective exchange interaction field and μ_{eff} is the average effective elementary moment involved in the FM–PM transition, their product $\mu_{eff} h_0$, i.e. the effective exchange energy, is expected to equal the thermal energy at $T = T_C$, i.e. $k_B T_C$. From table 1, it is obvious that, unless μ_{eff} is taken to be much larger than μ_0, this equality cannot hold. Hence, in order that the ratio $\mu_{eff} h_0/k_B T_C$ equals the 3D Heisenberg value of 1.58, μ_{eff} assumes the values listed in table 1. Moreover, the concentration of such effective moments is $c = \mu_0/\mu_{eff}$. The values of c, so computed and shown in table 1, indicate that only a small fraction of moments participates in the FM–PM phase transition. According to an earlier finding [3], the critical exponents assume smaller values with increasing Co concentration in the a-$Fe_{90-x}Co_xZr_{10}$ alloy series but they are still far greater than the 3D Heisenberg estimates. In contradiction to this result, the exponents β and γ *do not depend* on the alloy composition and possess 3D Heisenberg-like values. This implies that the transition at T_C is well defined and quenched disorder does not alter the critical behaviour of the pure spin system with specific heat critical exponent $\alpha_p < 0$, an inference in accordance with the well known Harris criterion. The Curie temperature T_C exhibits roughly a linear increase with increasing Co concentration, as previously reported [19] for a-$Fe_{90-x}Co_xZr_{10}$ alloys, presumably because the partial replacement of Fe with Co brings into play the strongly FM Fe–Co and Co–Co exchange interactions at the expense of *competing* Fe–Fe interactions. The concentration dependences of the quantities μ_0, c and T_C are depicted in figure 5. A glance at figure 5 reveals that the fraction c of the spins that actually participates in the FM–PM phase transition is small (about 11%) for the parent alloy a-$Fe_{90}Zr_{10}$ but increases with increasing Co concentration x as $c(x) - c(0) \simeq ax^2$, with $c(0) = 11 \pm 1\%$ and $a \simeq 0.25$, in the composition range investigated.

3.1.3. Ferromagnetic resonance linewidth. Temperature dependence of the 'peak-to-peak' FMR linewidth $\Delta H_{pp}(T)$ in the critical region ($|\epsilon| \lesssim 0.06$) for the glassy alloys in question observed in the $\|^h$ sample configuration is shown in figure 6. An important finding that deserves attention is that ΔH_{pp} has the same values (within the uncertainty limits, typically $\pm 10\%$) at any specified temperature in the critical region for both $\|^h$ and $\|^v$ sample configurations for a given composition in the a-$Fe_{90-x}Co_xZr_{10}$ alloy series. It turns out that the functional dependence of $\Delta H_{pp}(T)$ on temperature in the critical region for all compositions can very well be described by the empirical relation

$$\Delta H_{pp}(T) = A + B[M_S(T)]^{-1} \tag{6}$$

as is evident from the *linear* $\Delta H_{pp}(T)$ versus $[M_S(T)]^{-1}$ plots shown in figure 7. In view of equation (6) of I, the first and second terms in the above expression can be identified with the *frequency-independent* contribution $\Delta H_0(T)$ and *frequency-dependent* LLG contribution $\Delta H_{LLG}(\nu, T)$ $(= 1.45\lambda\omega/\gamma^2 M_S(T))$ to $\Delta H_{pp}(T)$. Recognizing the fact that M_S assumes small values in the critical region, $\Delta H_0(T)$ approaches a constant value A as $T \to T_C$ while the LLG damping mechanism gives a dominant contribution to $\Delta H_{pp}(T)$ in the critical region by virtue of its $[M_S(T)]^{-1}$ dependence. The Gilbert damping parameter λ for different compositions is calculated from the values of the coefficient B determined from the least-squares fits to the $\Delta H_{pp}(T)$ data based on equation (6). The *temperature-independent* values of λ, so computed and plotted against Co concentration in figure 5, range between 2×10^8 and 3.5×10^8 s^{-1}. In conformity with the earlier observation (I) that the parameter λ for a given composition does not depend on temperature, these values of λ (figure 5) are fairly close to those (figure 6 of I) deduced from the least-squares fits

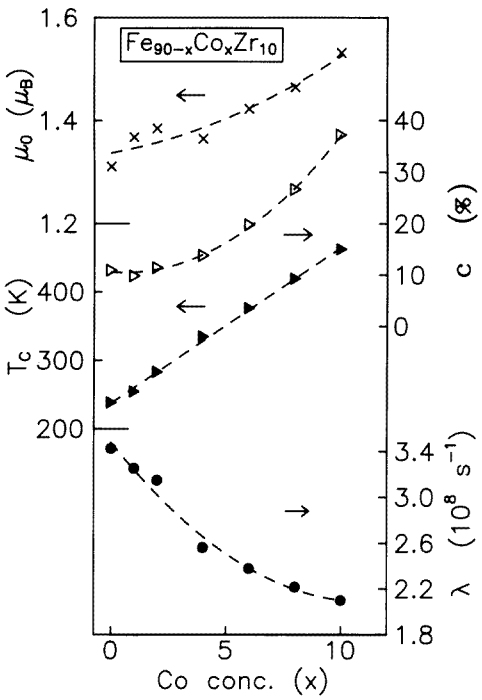

Figure 5. Functional dependences of the magnetic moment μ_0 per alloy atom at 0 K, the fraction c of spins participating in the FM–PM phase transition, the Curie temperature T_C and the Gilbert damping parameter λ on Co concentration x for a-Fe$_{90-x}$Co$_x$Zr$_{10}$ alloys. The dashed curves through the data points serve as a guide to the eye.

to the $\Delta H_{pp}(T)$ data over a wide temperature range based on equations (6) and (7) of I. A substantial decrease in the value of λ with increasing Co concentration in a-Fe$_{90-x}$Co$_x$Zr$_{10}$ alloys and its temperature-independent nature can be explained in the same way as in I and hence we need not elaborate that in this paper.

3.2. Uniaxial anisotropy field

3.2.1. Temperature dependence. The variation in the IP uniaxial anisotropy field H_k with temperature for different compositions in the a-Fe$_{90-x}$Co$_x$Zr$_{10}$ alloy series, depicted in figure 8, is deduced from the observed $H_{res}^{\parallel^h}(T)$ and $H_{res}^{\parallel^v}(T)$ (figure 2 of I) data using the relation (equation (3) of I)

$$H_k(T) = [H_{res}^{\parallel^v}(T) - H_{res}^{\parallel^h}(T)]/2. \tag{7}$$

A striking resemblance between the functional dependences of H_k and saturation magnetization M_S on temperature (cf figure 8 of this paper and figure 8 of I) strongly suggests a relation of the type

$$H_k(T) = \alpha M_S(T) \tag{8}$$

between H_k and M_S. Linear H_k versus M_S plots for the investigated compositions in the a-Fe$_{90-x}$Co$_x$Zr$_{10}$ alloy series displayed in figure 9 demonstrate that such a relation between H_k and M_S indeed holds in the present case over a wide temperature range. In order to

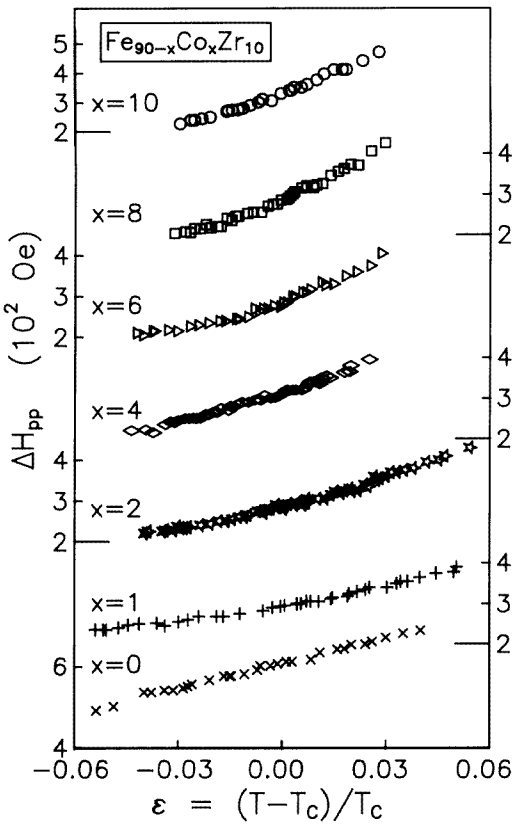

Figure 6. Temperature dependence of the 'peak-to-peak' FMR linewidth $\Delta H_{pp}(T)$ in the critical region ($|\epsilon| \lesssim 0.06$) for a-$Fe_{90-x}Co_xZr_{10}$ alloys in the horizontal-parallel configuration. Note that the ordinate scales on the left are for $x = 0$, 2, 6 and 10 whereas those on the right are for $x = 1$, 4 and 8; the longer horizontal bars mark the starting points on these scales.

demonstrate the composition dependence of H_k clearly, we compare the values of H_k for different compositions at fixed reduced temperatures T/T_C in figure 10. H_k increases with increasing Co concentration at a rate which is steep for $x \lesssim 2$ but progressively slows down as x is increased beyond $x = 4$. The overall functional dependence of H_k on x remains almost unaffected by changes in temperature. With the aid of the relation $H_k = 2K_u/M_S$ between H_k and the uniaxial anisotropy constant K_u, equation (8) can be rewritten in the form

$$K_u(T) = (\alpha/2)[M_S(T)]^2. \tag{9}$$

For a given composition in the glassy alloy series in question, values of K_u at different temperatures can be computed from equation (9) when the corresponding $M_S(T)$-values and the value of the slope α of the H_k versus M_S straight-line plot (figure 9), determined by the least-squares fit method, are inserted in equation (9). The compositional dependence of K_u at $T = 0.6T_C$, so obtained, is depicted in figure 11. The currently determined values of K_u are *typical* [16, 20–26] of amorphous 3d transition-metal (TM)-4d TM and 3d TM–metalloid alloys containing 80–90 at.% 3d TM, which exhibit long-range ferromagnetism.

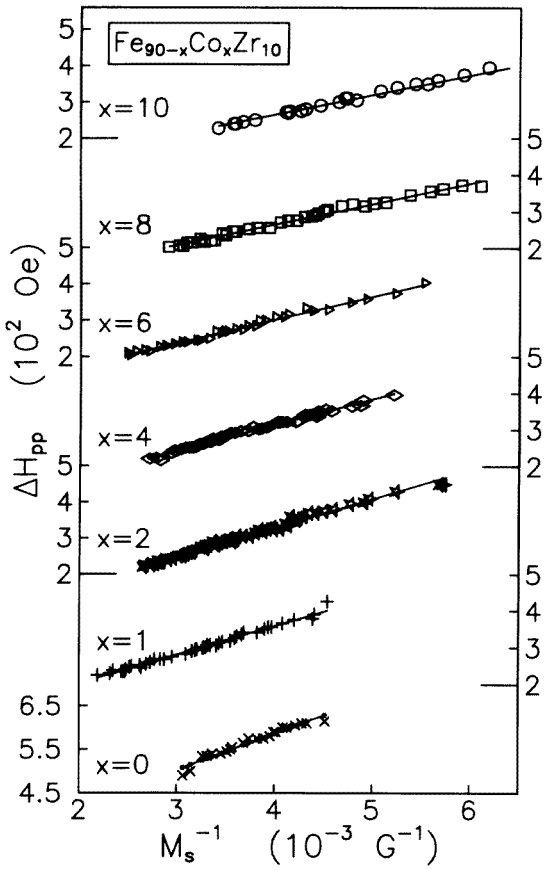

Figure 7. ΔH_{pp} plotted against inverse saturation magnetization in the temperature interval $-0.05 \lesssim \epsilon \lesssim 0.05$ for a-Fe$_{90-x}$Co$_x$Zr$_{10}$ alloys. The straight lines through the data points represent the least-squares fits to the data based on equation (6) of the text. Note that the ordinate scales on the left are for $x = 0$, 2, 6 and 10 whereas those on the right are for $x = 1$, 4 and 8; the longer horizontal bars mark the starting points on these scales.

3.2.2. Composition dependence. With a view to testing the validity of the assumption $H_k \ll 4\pi M_S$ (on which equation (7) rests) and hence to ascertaining whether or not equation (7) determines H_k accurately, we have extracted values of H_k for different compositions at $T = 0.6T_C$ from the angular dependence of the resonance field using the method mentioned below. The rationale behind the choice of this temperature is that the angular dependence of the primary resonance can be studied without any interference [15] from the secondary resonance, which makes its presence felt at $T \simeq T_C$. Figure 12 shows the PAD curves plotted against the external field H for a few specified angles that H makes with the easy axis in the IP and OP configurations at $T = 0.6T_C$ for the primary resonance in a-Fe$_{88}$Co$_2$Zr$_{10}$ alloy. The angular variation in the PAD curves displayed in figure 12 is also *characteristic* of other compositions in the glassy alloy series investigated. The angular dependence of H_{res} and ΔH_{pp} for the two geometries, deduced for the $\mathrm{d}P/\mathrm{d}H$ versus H curves (figure 12), is depicted in figures 13 and 14, respectively. It is evident from figure 13 that the change in H_{res} in the IP case as the angle ψ is swept through 90° is of the

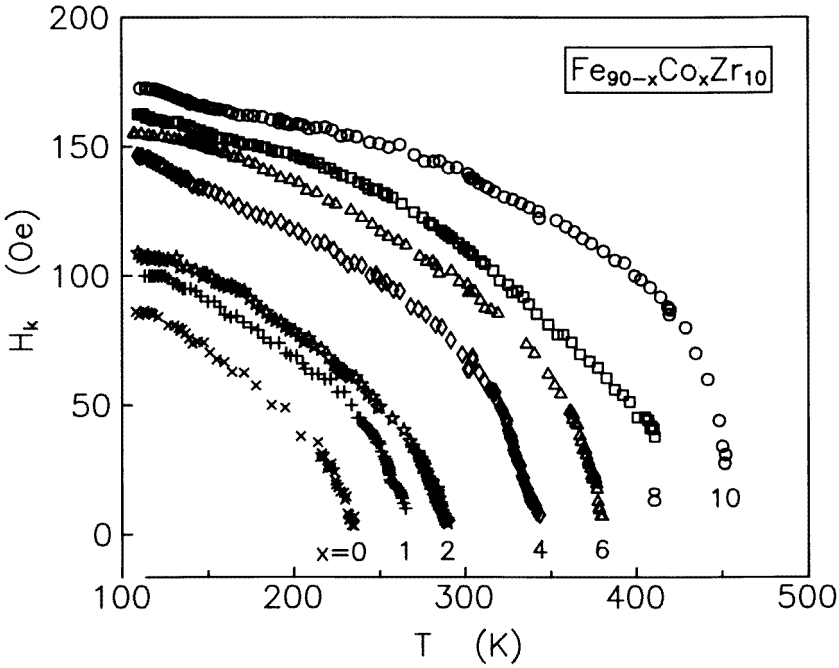

Figure 8. Variation in the IP uniaxial anisotropy field H_k with temperature for a-$Fe_{90-x}Co_xZr_{10}$ alloys.

order of a few hundred oersteds while H_{res} changes by more than an order of magnitude from its value at $\alpha = 0^\circ$ when $\alpha \to 90^\circ$ in the OP case. Similar variation with the angles ψ and α is also observed for ΔH_{pp} (figure 14). Absence of $H_{res}(\alpha)$ and $\Delta H_{pp}(\alpha)$ data points for angles in the vicinity of 90° in figures 13(b) and 14(b) should not be interpreted as a signature of divergence but instead, for angles $\alpha \simeq 90^\circ$, both H_{res} and ΔH_{pp} exceed the highest magnetic field (about 11 kOe) generated by the electromagnet coupled to the spectrometer. In figure 13, the continuous curves denote the variation in H_{res} with the angle ψ or α yielded by the theoretical calculations whose gist is given below.

With the choice of the coordinate system as shown in figure 15, the free-energy density for a thin film with an IP uniaxial anisotropy field $H_k = 2K_u/M_S$ directed along the x axis (easy axis) is given by

$$E = -M_S H(\sin\theta_M \sin\theta_H \cos(\phi_H - \phi_M) + \cos\theta_M \cos\theta_H) + 2\pi M_S^2 \cos^2\theta_M + K_u(1 - \sin^2\theta_M \cos^2\phi_M) \tag{10}$$

where M_S is the saturation magnetization, θ_M, θ_H and ϕ_M, ϕ_H are the customary angles defining the directions of the magnetization vector $\boldsymbol{M}_S$ and the external magnetic field vector $\boldsymbol{H}$ in spherical polar coordinates (figure 15). In the above expression, the first, second and third terms are the Zeeman, demagnetizing and uniaxial anisotropy contributions to the free-energy density, respectively. Following the standard approach [27], the equilibrium conditions for magnetization at resonance, i.e.

$$H_{res}[\sin\theta_M \cos\theta_H - \cos\theta_M \sin\theta_H \cos(\phi_H - \phi_M)] = 2\pi M_S \sin(2\theta_M) + (H_k/2)\sin(2\theta_M)\cos^2\phi_M \tag{11}$$

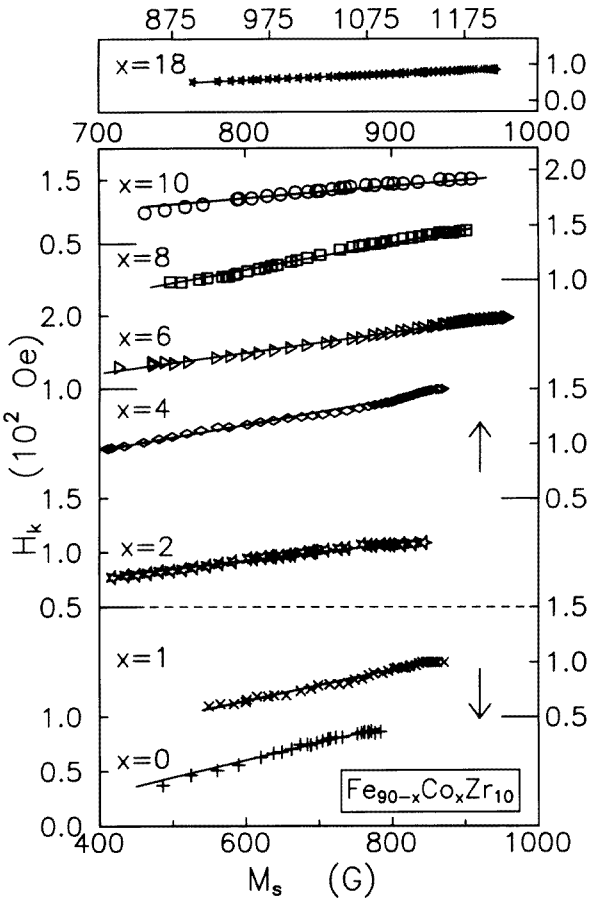

Figure 9. $H_k(T)$ plotted against $M_S(T)$ in the temperature range 77 K $\leqslant T \lesssim T_C$ (77 K $\leqslant T \leqslant$ 500 K) for a-Fe$_{90-x}$Co$_x$Zr$_{10}$ alloys with $x = 0$, 1, 2, 4, 6, 8 and 10 ($x = 18$). The straight lines through the data points represent the best least-squares fits to the data based on equation (18) of the text. Note that the ordinate scales on the left are for $x = 0$, 2, 6 and 10 whereas those on the right are for $x = 1$, 4 and 8; the longer horizontal bars mark the beginning of these scales.

and

$$H_{res} \sin\theta_H \sin(\phi_H - \phi_M) = (H_k/2) \sin\theta_M \sin(2\theta_M) \tag{12}$$

and the resonance condition

$$\begin{aligned}(\omega/\gamma)^2 = {} & [H_{res}\{\cos\theta_M \cos\theta_H + \sin\theta_M \sin\theta_H \cos(\phi_H - \phi_M)\} \\ & -(4\pi M_S + H_k \cos^2\phi_M)\cos(2\theta_M)] \\ & \times[H_{res}\{\cos\theta_M \cos\theta_H + \sin\theta_M \sin\theta_H \cos(\phi_H - \phi_M)\} \\ & -(4\pi M_S + H_k \cos^2\phi_M)\cos^2\theta_M + H_k \cos(2\phi_M)] \\ & -((H_k/2)\cos\theta_M \sin(2\phi_M))^2\end{aligned} \tag{13}$$

are obtained using the relations [27]

$$\frac{\partial E}{\partial \theta_M} = 0 \tag{14}$$

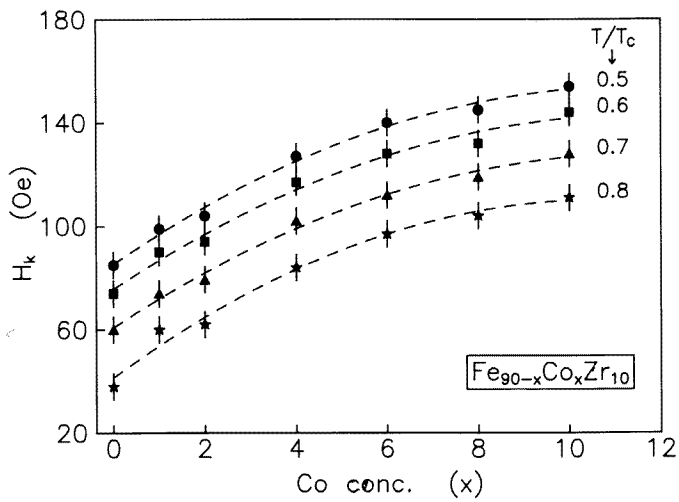

Figure 10. Co concentration dependence of H_k at a few representative values of the reduced temperature T/T_C.

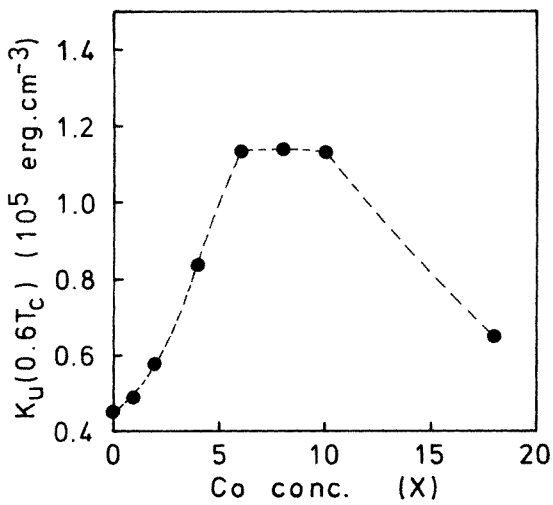

Figure 11. Variation in the uniaxial anisotropy constant K_u with Co concentration at $T = 0.6T_C$ in a-$Fe_{90-x}Co_xZr_{10}$ alloys.

$$\frac{\partial E}{\partial \phi_M} = 0 \tag{15}$$

and

$$\left(\frac{\omega}{\gamma}\right)^2 = \frac{1}{M_S^2 \sin^2\theta_M}\left[\frac{\partial^2 E}{\partial \theta_M^2}\frac{\partial^2 E}{\partial \phi_M^2} - \left(\frac{\partial^2 E}{\partial \theta_M \partial \phi_M}\right)^2\right] \tag{16}$$

respectively. Note that, in equations (11)–(16), θ_M and ϕ_M denote the equilibrium values of these angles for a given direction of $\boldsymbol{H}$, which is specified by the angles θ_H and ϕ_H. In the OP configuration (figure 16(*a*)), both $\boldsymbol{H}$ and $\boldsymbol{M}_S$ are confined to the x–z plane so that

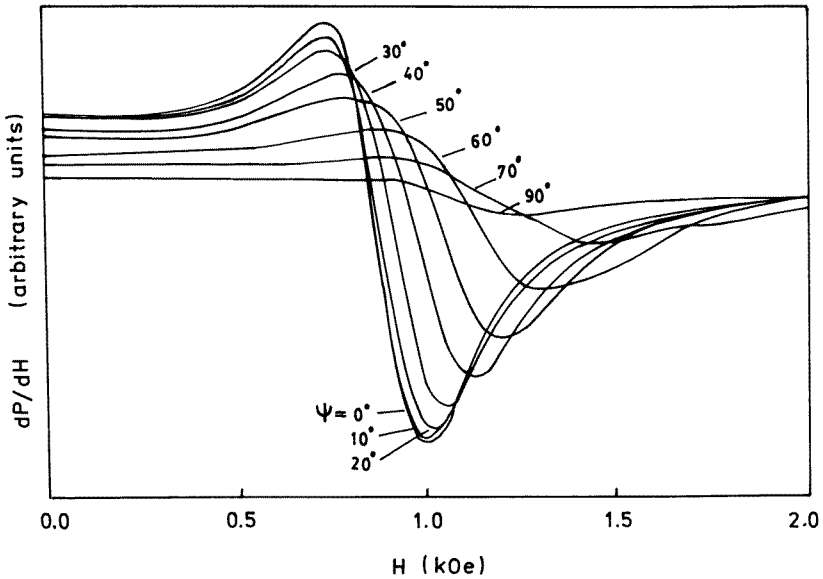

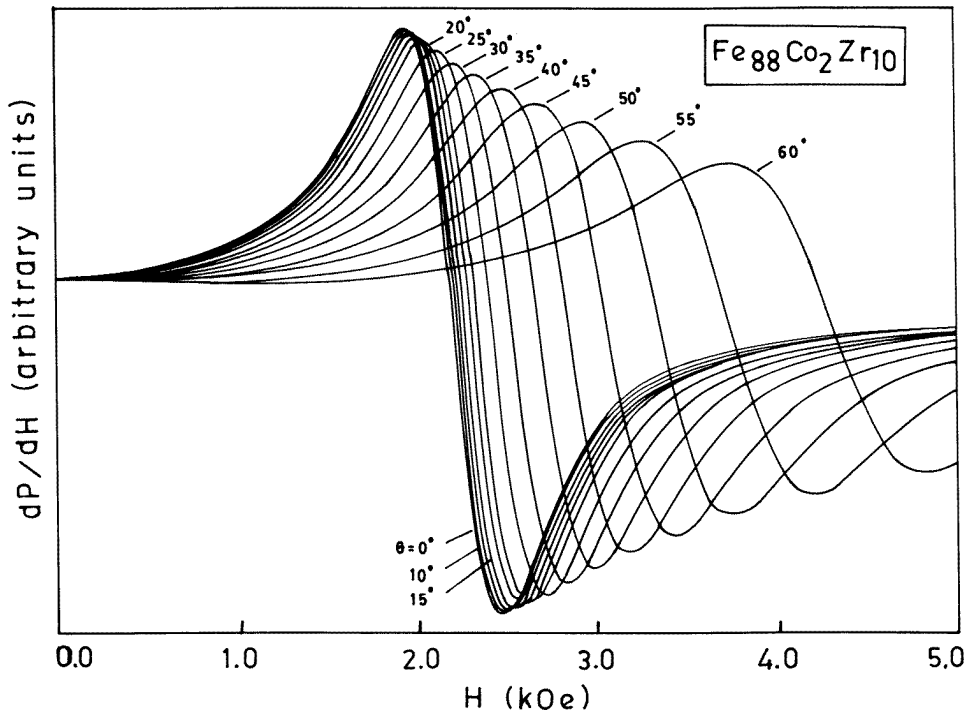

Figure 12. Power absorption curves for a few specified angles that the static magnetic field H makes with the easy axis in the IP and OP configurations at $T = 0.6T_C$ a-$Fe_{88}Co_2Zr_{10}$ alloy.

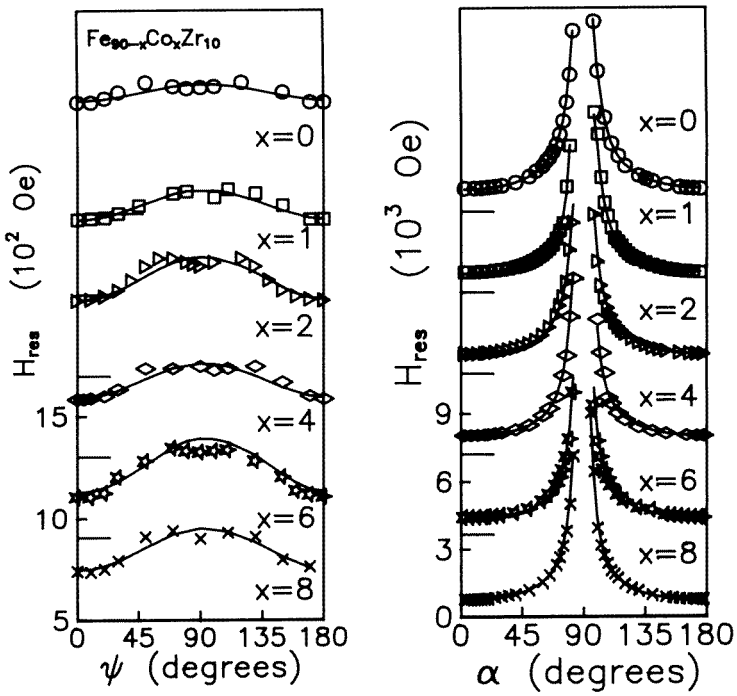

Figure 13. Variations in the resonance field H_{res} with the angles ψ and α for the IP and OP cases, respectively, in a-$Fe_{90-x}Co_xZr_{10}$ alloys at $T = 0.06T_C$. The continuous curves through the data points for the IP and OP cases are the best least-squares fits to the data based on equations (20) and (18), respectively, of the text. Note the shift in the origin (long bars) of the ordinate scale for Co concentrations ranging from 0 to 6.

$\phi_M = \phi_H = 0$ and the angles θ_M and θ_H are measured with respect to the z axis which lies in the sample plane (y–z plane) along the easy axis, i.e. $\theta_M = \pi/2 - \theta$ and $\theta_H = \pi/2 - \alpha$. In this case, equations (11) and (13) take the form

$$\frac{\sin\alpha}{\sin\theta} - \frac{\cos\alpha}{\cos\theta} - \frac{4\pi M_S + H_k}{H_{res}} = 0 \tag{17}$$

and

$$(\omega/\gamma)^2 = [H_{res}\cos(\alpha-\theta) + (4\pi M_S + H_k)\cos 2\theta] \times [H_{res}\cos(\alpha-\theta) - 4\pi M_S \sin^2\theta + H_k\cos^2\theta]. \tag{18}$$

By contrast, the vectors $\boldsymbol{H}$ and $\boldsymbol{M}_S$ are confined to the sample plane (y–z plane), i.e. $\theta_M = \theta_H = \pi/2$ in the IP configuration (figure 16(b)) and the angles ϕ_M and ϕ_H are measured with respect to the easy axis (z axis) in the sample plane such that $\phi_M \equiv \phi$ and $\phi_H \equiv \psi$. In the IP case, equations (12) and (13) thus reduce to

$$\frac{\sin\psi}{\sin\phi} - \frac{\cos\psi}{\cos\phi} - \frac{H_k}{H_{res}} = 0 \tag{19}$$

and

$$(\omega/\gamma)^2 = [H_{res}\cos(\psi-\phi) + 4\pi M_S + H_k\cos^2\phi][H_{res}\cos(\psi-\phi) + H_k\cos(2\phi)]. \tag{20}$$

For a given direction of $\boldsymbol{H}_{res}$ represented by a certain value of the angle ψ (α) in the IP (OP) case, the equilibrium value of the (magnetization) angle ϕ (θ) and the values of M_S

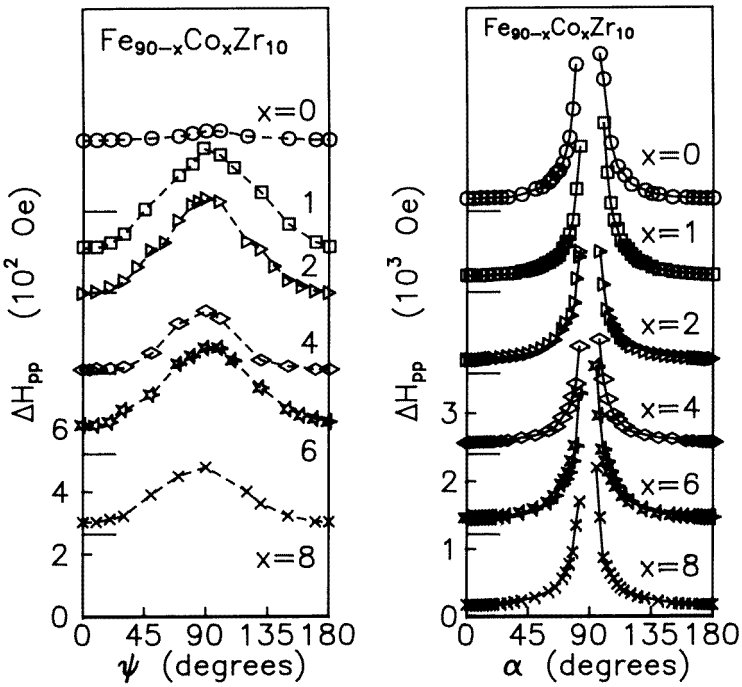

Figure 14. Functional dependences of the FMR linewidth ΔH_{pp} on the angles ψ and α for the IP and OP cases, respectively, in a-Fe$_{90-x}$Co$_x$Zr$_{10}$ alloys at $T = 0, 6T_C$. Note the shift in the origin (long bars) of the ordinate scale for Co concentrations ranging from 0 to 6. The curves through the data points serve to highlight the angular variation.

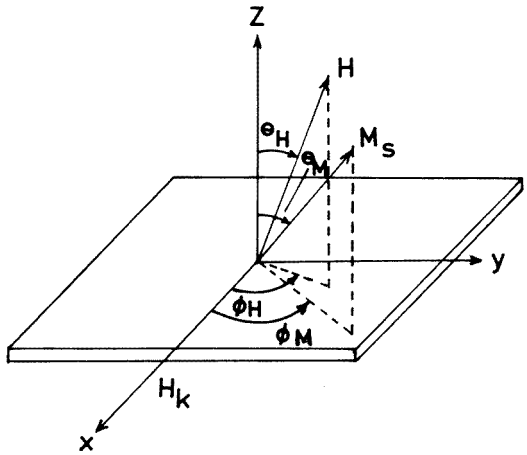

Figure 15. The coordinate system for a thin film with an IP uniaxial anisotropy.

and H_k for each composition are self-consistently calculated from equations (19) and (20) (equations (17) and (18)) using the experimentally observed value of $H_{res}(\psi)$ ($H_{res}(\alpha)$).

Values of θ, so computed, are plotted against α for all the investigated compositions in

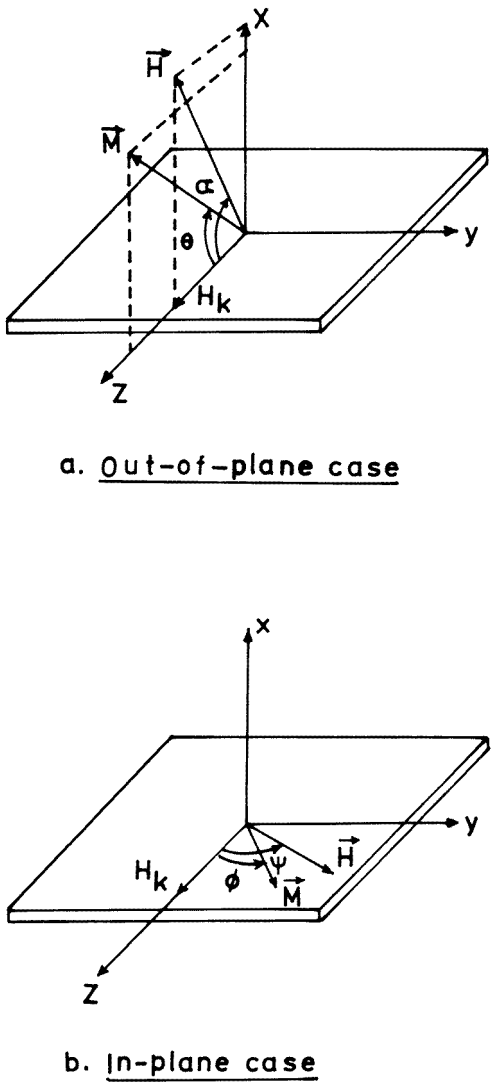

Figure 16. Coordinate systems showing various angles used in the computation of angular variation of the resonance field for (*a*) OP and (*b*) IP configurations.

the glassy alloy series a-$Fe_{90-x}Co_xZr_{10}$ in figure 17. A similar plot for the IP case, i.e. the ϕ versus ψ plot, is not shown because these plots are straight lines with slope equal to unity (i.e. $\phi \simeq \psi$) for all the values of the Co concentration x. Alternatively, the ϕ versus ψ data for all the compositions fall on a *universal* straight line whose slope equals unity. In view of equation (19), the observation that $\phi \simeq \psi$ is a consequence of the fact that $H_k \ll H_{res}$. This result implies that for any direction of the external static magnetic field in the sample plane, H_{res} greatly exceeds both the demagnetizing field (which is negligibly small, about 100 Oe or less, in the IP configuration) as well as H_k and hence the direction of $\boldsymbol{M}_S$ coincides with that of $\boldsymbol{H}_{res}$. On the other hand, in the OP case, the increase in θ is only marginal (from 0° to about 5°) in the interval $0° \leqslant \alpha \leqslant 45°$ but picks up abruptly for values

of α in the range 70–90° and the 'knee' in the θ versus α curves (figure 17) shifts to *higher* values of α with increasing Co concentration. These features of the θ versus α curves can be understood as follows. For angles α ranging between 0° and 45°, the magnetization vector $\boldsymbol{M}_S$ is unable to keep pace with the alterations in the static magnetic field direction because the angle θ between $\boldsymbol{M}_S$ and $\boldsymbol{H}_{res}$ as well as $|\boldsymbol{H}_{res}|$ are small and hence the torque experienced by $\boldsymbol{M}_S$ due to $\boldsymbol{H}_{res}$ is not strong enough to counter the tendency of both shape and uniaxial anisotropies to confine $\boldsymbol{M}_S$ to the sample plane. As a consequence, θ possesses small values in this range of α. By contrast, when α lies between 70° and 90°, both θ and $|\boldsymbol{H}_{res}|$ attain large values (figure 13) and the torque exerted by $\boldsymbol{H}_{res}$ on $\boldsymbol{M}_S$ is now able to work effectively against the dictates of the anisotropies in question (particularly the shape anisotropy energy which assumes large values for α in the vicinity of 90°) and cause a sizable change in the direction of $\boldsymbol{M}_S$ with the result that θ increases abruptly. In view of this explanation, the displacement of the 'knee' to higher values of α with increasing Co concentration x is a manifestation of the fact that both demagnetizing and uniaxial anisotropy energies increase in magnitude as M_S and H_k increase with increasing x. The values of M_S and H_k, self-consistently calculated from equations (17)–(20) and plotted against x in figure 18, clearly demonstrate this trend. Moreover, close scrutiny of the data presented in figures 10 and 18 reveals that excellent agreement exists between the sets of values for $M_S(x)$ and $H_k(x)$ at $T = 0.6T_C$ obtained from the temperature and angular dependences of H_{res} and that, in conformity with the observation $H_k(T) \propto M_S(T)$ (figure 9), $H_k(x)$ scales with $M_S(x)$ at $T = 0.6T_C$ (figure 18). While the present finding that H_{res} as a function of the angle ψ (α) goes through a maximum at $\psi = 90°$ ($\alpha = 90°$) and minima at $\psi = 0°$ and 180° ($\alpha = 0°$ and 180°) asserts that the anisotropy is of a uniaxial nature, the observation that $H_k(x, T)$ scales with $M_S(x, T)$ strongly indicates that the uniaxial anisotropy in the amorphous alloys investigated at present has its origin in the pseudo-dipolar atomic pair ordering [25, 26], which develops during the rapid melt-quenching process.

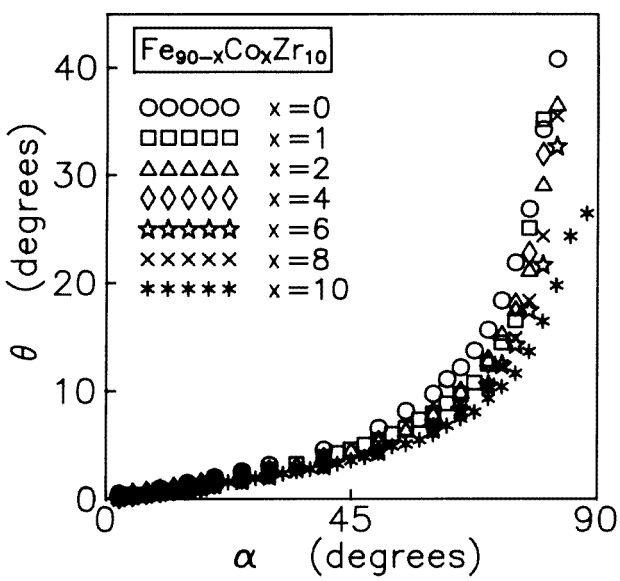

Figure 17. Variation in the magnetization angle θ with α, the angle between the external static magnetic field and the sample plane, in the OP configuration at $T = 0.6T_C$.

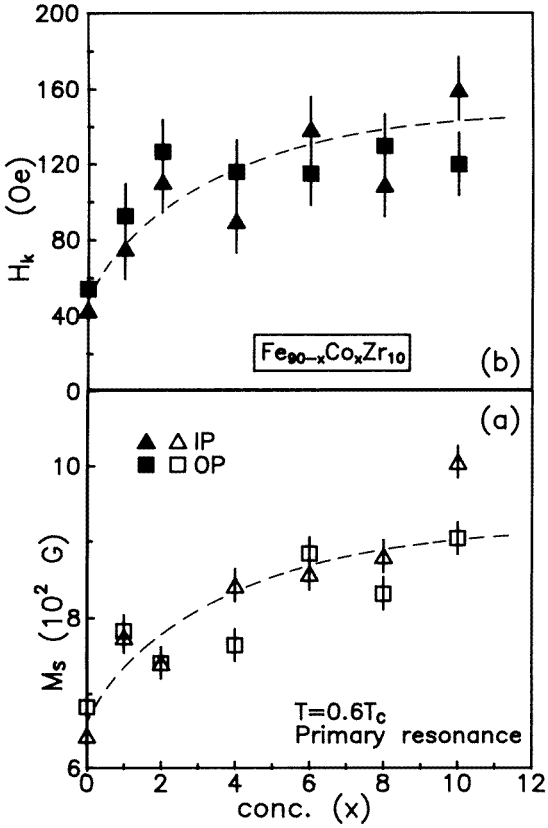

Figure 18. Dependences of (*a*) M_S and (*b*) H_k on Co concentration x.

While discussing the angular dependence of the FMR linewidth, two points need serious consideration. First, as the frequency of the microwave field is held constant and the applied static magnetic field H_a is swept through resonance in the present experiments, corrections have to be made for the fact that $\boldsymbol{M}$ and $\boldsymbol{H}_a$ are not collinear, so that the change in the applied field is not the same as the change in the *effective* field H_e. Second, as H_a changes, the direction of $\boldsymbol{M}$ changes, giving rise to an apparent line broadening which must also be taken into account. Such corrections are small in the IP case since the angles in question are small. However, in the OP case, $\boldsymbol{M}$ goes out of the sample plane, the demagnetizing fields are large and corrections to the 'raw' linewidth data are necessary. The intrinsic, or effective field, linewidth ΔH_e is related to the measured linewidth ΔH_a ($\equiv \Delta H_{pp}$), as [28]

$$\Delta H_e = \left(\frac{\partial H_e}{\partial H_a}\right)_{res} \Delta H_a + \left(\frac{\partial H_e}{\partial \theta}\right)_{res} \Delta\theta \tag{21}$$

where the two partial derivatives, evaluated at resonance, i.e. at $H_e = \omega/\gamma$ and $H_a = H_{res}$, are obtained from equation (18). Note that equation (21) holds for the OP case and a similar relation for the IP case is obtained by replacing θ in equation (21) by ϕ. In the latter case, the partial derivatives are computed using equation (20). Since H_a and θ (ϕ) are related through the equilibrium condition equation (17) (equation (19)), equation (21)

and its counterpart for the IP case can be expressed as [29]

$$\Delta H_e = \left(\frac{\mathrm{d}H_e}{\mathrm{d}H_a}\right)_{res} \Delta H_a. \tag{22}$$

In view of the equations (17)–(22), it is not surprising that the variations in ΔH_{pp} ($\equiv \Delta H_a$) with angles ψ and α are similar to those of H_{res} (cf figures 13 and 14).

4. Summary and conclusions

Elaborate analysis of the FMR data taken in the critical region on amorphous $Fe_{90-x}Co_xZr_{10}$ ($0 \leqslant x \leqslant 10$) alloys and that of the observed temperature and angular dependences of the resonance field for different compositions in this series permit us to draw the following conclusions.

(i) An accurate determination of the critical exponents β and γ for the spontaneous magnetization and initial susceptibility that characterize the FM–PM phase transition is possible using the FMR technique.

(ii) Contrary to the earlier claim [3], the critical exponents β and γ are *composition independent* and possess values that are close to the theoretical estimates [17] for an isotropic short-range 3D Heisenberg ferromagnet. Alternatively, in accordance with the well known Harris criterion, the quenched disorder does not change the critical behaviour of a 3D *ordered* spin system whose specific heat critical exponent is *negative*.

(iii) While the values of the amplitude ratio $m_0/M_S(0)$ are consistent with the Harris criterion, the ratio $\mu_0 h_0/k_B T_C$ has values that are *composition dependent* and an order of magnitude smaller than the 3D Heisenberg value of 1.58. The latter discrepancy between experiment and theory is shown to imply that only a small fraction (about 11% for $Fe_{90}Zr_{10}$) of spins is actually participating in the FM–PM phase transition and that this fraction c increases with increasing x as $c(x) - c(0) \simeq ax^2$.

(iv) In the critical region, the LLG relaxation is primarily responsible for the observed FMR linewidth ΔH_{pp}. This is borne out by the observation that $\Delta H_{pp}(T) \propto [M_S(T)]^{-1}$ in the critical region.

(v) Consistent with the results obtained in a wide temperature range [15], which embraces the critical region, the Landé splitting factor g has a temperature- and composition-independent value of 2.07 ± 0.02 while the Gilbert damping parameter λ, although temperature independent, decreases with increasing Co concentration.

(vi) The variations in the IP uniaxial anisotropy field $H_k = 2K_u/M_S$ with temperature and composition, deduced from the temperature dependence of the resonance field in the horizontal-parallel and vertical-parallel sample configurations and from the angular dependence of the resonance field observed in both IP and OP sample geometries, respectively, at $T = 0.6T_C$, demonstrate that $H_k(x,t)$ *scales* with $M_S(x,T)$. This observation, in turn, strongly suggests that the uniaxial anisotropy originates from the pseudo-dipolar atomic pair ordering which develops during the rapid melt-quenching process.

References

[1] Hiroyoshi H, Fukamichi K, Hoshi A and Nakagawa Y 1983 *High Field Magnetism* ed M Date (Amsterdam: North-Holland) p 113
[2] Yamauchi H, Onodera H and Yamamoto H 1984 *J. Phys. Soc. Japan* **53** 747
[3] Winschuh K and Rosenberg M 1987 *J. Appl. Phys.* **61** 4401

[4] Reisser R, Fähnle M and Kronmüller H 1988 *J. Magn. Magn. Mater.* **75** 45
[5] Kaul S N 1988 *J. Phys. F: Met. Phys.* **18** 2089
[6] Kaul S N, Hofmann A and Kronmüller H 1986 *J. Phys. F: Met. Phys.* **16** 365
Kaul S N 1987 *J. Appl. Phys.* **61** 451
[7] Ma H, Kunkel H P and Williams G 1991 *J. Phys.: Condens. Matter* **3** 5563
[8] Pureur P, Schreiner W H, Kunzler J V, Ryan D H and Coey J M D 1988 *Solid State Commun.* **65** 163
[9] Mohan Ch V, Babu P D, Sambasiva Rao M, Lucinski T and Kaul S N 1993 *Proc. Int. Conf. on Disordered Materials* ed S K Srivastava (Allahabad: Poonam Press) p 158
[10] Rhyne J J and Fish G E 1985 *J. Appl. Phys.* **57** 3407
[11] Rhyne J J, Erwin R W, Fernandez-Baca J A and Fish G E 1988 *J. Appl. Phys.* **63** 4080
[12] Kaul S N and Mohan Ch V 1991 *J. Phys.: Condens. Matter* **3** 2703
[13] Kaul S N and Babu P D 1992 *Phys. Rev.* B **45** 295
[14] Kaul S N and Mohan Ch V 1992 *J. Appl. Phys.* **71** 6103
[15] Siruguri V and Kaul S N 1996 *J. Phys.: Condens. Matter* **8** 4545
[16] Kaul S N and Siruguri V 1992 *J. Phys.: Condens. Matter* **4** 505
[17] LeGuillou L C and Zinn-Justin J 1980 *Phys. Rev.* B **21** 3976
[18] Kaul S N 1985 *J. Magn. Magn. Mater.* **53** 5
[19] Deppe P, Fukamichi K, Li F S, Rosenberg M and Sostarich M 1984 *IEEE Trans. Magn.* **20** 1367
[20] Hasegawa R 1975 *Proc. 21st Annual Conf. on Magnetism and Magnetic Materials* ed J J Becker, G H Lander and J J Rhyne (New York: American Institute of Physics) p 216
[21] Hasegawa R, O'Handley R C and Mendelsohn L T 1976 *Magnetism and Magnetic Materials 1976, Proc. 1st Joint MMM–Intermag. Cong.* ed J J Becker and G H Lander (New York: American Institute of Physics) p 298
[22] Luborsky F E and Walter J L 1977 *IEEE Trans. Magn.* **13** 1635
[23] Takahashi M and Kim C O 1978 *Japan. J. Appl. Phys.* **16** 206
[24] Luborsky F E 1980 *Ferromagnetic Materials* vol 1, ed E P Wohlfarth (Amsterdam: North-Holland) p 451
[25] Fujimori H 1983 *Amorphous Metallic Alloys* ed F E Luborsky (London: Butterworth) p 300
[26] Ounadjela K, Suran G and Machizaud F 1989 *Phys. Rev.* B **40** 570
[27] Smit J and Beljers H G 1955 *Philips Res. Rep.* **10** 113
Suhl H 1955 *Phys. Rev.* **97** 555
[28] Vittoria C, Barker R C and Yelon A 1967 *Phys. Rev. Lett.* **19** 792
[29] Sparks M 1964 *Ferromagnetic Relaxation Theory* (New York: McGraw-Hill) p 27